



CHORUS

This is the accepted manuscript made available via CHORUS. The article has been published as:

T-matrix evaluation of three-dimensional acoustic radiation forces on nonspherical objects in Bessel beams with arbitrary order and location

Zhixiong Gong, Philip L. Marston, and Wei Li

Phys. Rev. E **99**, 063004 — Published 25 June 2019

DOI: [10.1103/PhysRevE.99.063004](https://doi.org/10.1103/PhysRevE.99.063004)

1 **T-matrix evaluation of three-dimensional acoustic radiation forces on nonspherical**
2 **objects in Bessel beams with arbitrary order and location**

3 Zhixiong Gong^{1,2,†}, Philip L. Marston^{2,‡}, Wei Li^{1,*}

4 ¹School of Naval Architecture and Ocean Engineering, Huazhong University of Science
5 and Technology, Wuhan 430074, China

6 ²Department of Physics and Astronomy, Washington State University, Pullman,
7 Washington 99164-2814, United States

8 † Present address: Univ. Lille, CNRS, Centrale Lille, ISEN, Univ. Polytechniques
9 Hauts-de-France, UMR 8520-IEMN, International laboratory LIA/LICS, F-59000 Lille,
10 France

11 zhixiong.gong@iemn.fr

12 ‡ marston@wsu.edu

13 * Corresponding author: hustliw@hust.edu.cn

14
15 Acoustic radiation forces (ARFs) induced by a single Bessel beam with arbitrary order
16 and location on a nonspherical shape are studied using the T-matrix method (TMM) in
17 three dimensions. Based on the radiation stress tensor approach and the multipole
18 expansion method for the arbitrary Bessel beam, the ARF expressions are derived in
19 terms of the incident and scattered beam shape coefficients independently with the
20 corresponding homemade code packages. Several numerical experiments are conducted
21 to verify the versatility of the TMM. The axial acoustic radiation forces (ARFs) of several
22 typical shapes are considered in the analysis with the emphasis on the axial ARF reversal

23 and the corresponding physical mechanism. This study may guide the experimental set-up
24 to find negative axial ARFs quickly and effectively based on the predicted parameters
25 with TMM. Relatively elongated shapes may be helpful for pulling forces in Bessel
26 beams. Furthermore, the lateral ARFs for both convex and concave nonspherical shapes
27 are also investigated with different topological charges, cone angles and offsets of the
28 particle centroid to the beam axis in a broadband frequency regime. A brief theoretical
29 derivation of the incident beam shape coefficients for the standing Bessel beams is also
30 given. The present work could help to design the acoustic tweezers numerical toolbox
31 which provides an acoustical alternative to the optical tweezers toolbox.

32 **1 Introduction**

33 Acoustic tweezers¹⁻⁴, an appropriate counterpart to optical tweezers⁵, could be used for
34 levitation^{6,7}, pulling forces⁸⁻¹², particle trapping^{13,14}, and even dynamic controls^{15,16} in the
35 fields of microfluidics and life sciences. Compared with optic tweezers, acoustic tweezers
36 tend to exert a larger force over larger length scales with the same intensity since the
37 radiation force is proportional to the ratio of the intensity to the velocity in the medium^{2,17}.
38 In general, there are two main schemes to design acoustic tweezers: the (quasi)standing
39 wave scheme with dual beams^{1,2,4} and the single beam structure³. Single-beam tweezers
40 may be superior to general plane standing-wave tweezers in some respects, for instance,
41 single-beam tweezers can continuously pull or push a particle over a large region because
42 there are no multiple equilibrium positions^{10,17}. Negative radiation force single-beam

43 device could pull the target towards the source, which is of interest in both
44 acoustical^{8-12,17} and optical fields¹⁸. The physical mechanism is due to the asymmetric
45 scattering of the incident fields on the target such that the scattering into the forward
46 direction is relatively stronger than the scattering into the backward direction^{8-10,18,19}. This
47 is understood by the conservation of momentum and Newton's third law regarding
48 reaction force between the acoustic field and the inside particle.^{19,20}

49 Beams having the local properties of acoustic Bessel beams are candidates for
50 single-beam tweezers which have been examined in theoretical^{8-10,21} and experimental
51 approaches^{17,22}. The ordinary Bessel beam (OBB) possesses the axial maximum and
52 azimuthal symmetry, while the helicoidal Bessel beams (HBBs) have an axial null and
53 azimuthal phase gradient. Hefner and Marston conducted the experimental demonstration
54 for the acoustical vortices by using simple four-panel piezoelectric transducers²³.
55 Recently, the transducer arrays^{17,24}, active spiral transducer^{25,26}, diffraction gratings²⁷ and
56 metasurfaces²⁸ have been demonstrated to produce the local Bessel beams which coincide
57 with the theoretical or simulation results. These fabrication technologies facilitate the
58 experimental studies of Bessel beams and the possible applications in the fields of
59 particle manipulations. In addition, the exact series solutions have been solved for the
60 axial ARFs of *spherical* objects in an on-axis incident Bessel beam for both the
61 ordinary^{8,9} and helicoidal (vortex)^{10,17} Bessel beams. The ARF produced by a Bessel
62 vortex beam has also been studied via the optical theorem²⁹⁻³³ which gives the

63 relationship between the extinction and the scattering at the forward direction of the
64 beam's plane wave components. However, it is still necessary to develop efficient and
65 versatile numerical models to investigate the three-dimensional ARFs of particles with
66 different shapes and other complicated conditions.

67 To this end, the T-matrix method (TMM) is introduced to the field of acoustic
68 manipulations which has been demonstrated effective and very efficient for acoustic
69 scattering³⁴ from spheroid³⁵⁻³⁸, superspheroid^{38,39} and finite cylinder with endcaps^{40,41}.
70 These nonspherical (convex or concave) shapes are very common to model the
71 geometries of particles in biomedical engineering (e.g., cells and bacteria) and lab-chip
72 technologies (e.g., drops with gravity and fibers) in the context of acoustophoresis, which
73 could provide more accurate models and give a better prediction of the particle motions
74 than the spherical shape. It is noteworthy that other numerical methods, such as the finite
75 element method^{42,43}, boundary element method⁴⁴⁻⁴⁶, finite volume method^{47,48}, lattice
76 Boltzmann method^{49,50} and finite-difference time-domain method⁵¹, are also employed to
77 successfully solve the acoustic radiation force of particles in fluid. Each numerical
78 methods has its own metrics. However, for typical axisymmetric shapes, the TMM will
79 be a superior approach since it will decrease the integral over the geometrical surface
80 (three dimensions) into the line integral (two dimensions) and could save much
81 computational cost, leading to high efficiency in the simulation experiments even at high
82 frequencies^{38,39}. Furthermore, based on the radiation stress tensor approach^{52,29} and the

83 independent derivations, the three-dimensional ARFs could be expressed and calculated
84 in terms of the incident and scattered beam shape coefficients (see details below). Note
85 that the transition matrix need only to calculate once for the scattered field and is
86 independent of the incident beams, making the TMM even more efficient to calculate the
87 forces on particles. It is convenient to obtain the incident beam shape coefficients for the
88 ordinary and standing plane wave, however, may be challenging in the context of vortex
89 beam since the particle may deviate the beam axis with an offset. For an ideal Bessel
90 beam of arbitrary topological charge and location, general theoretical formulas of the
91 incident beam shape coefficients are derived based on the multipole expansion method³⁵
92 and also given by Zhang⁵³.

93 It is important to investigate the particle dynamics in three dimensions with the on-
94 or off-axis incidence since it could help the beam calibrate with the particle centroid in
95 experimental setups with higher frequency regime. To some extent, the numerical method
96 is an alternative to direct experimental approaches and more versatile than analytical
97 investigations. In this paper, several numerical experiments are conducted based on the
98 traditional T-matrix method with the emphasis on *nonspherical* objects which are typical
99 in engineering practice and life sciences, such as the generalized superspheroid and finite
100 cylinder with endcaps which may be used to model the biological cells or bacteria. This
101 will extend the previous theoretical studies of the axial ARF⁸⁻¹⁰ and numerical
102 implementations of the off-axial ARF on a sphere^{54,11} to cases of an object with

103 complicate shapes placed in a Bessel beam with arbitrary location and order. Note that
104 Few analytical solutions of the ARF on rigid spheroids have been derived in the
105 long-wavelength limit^{55,56}, which has the potential for the Bessel beam illumination
106 example. The physical mechanism of the axial ARF reversal for nonspherical shape is
107 demonstrated by numerical experiments and the corresponding parameter conditions are
108 discussed. In addition, the lateral and the axial ARFs for both convex and concave
109 nonspherical shapes are discussed with emphasis on the dimensionless frequency, the
110 cone angle of the Bessel beam and the offsets. The theoretical formulas of the Bessel
111 standing wave with arbitrary orders and offsets are also briefly given with the numerical
112 example.

113 **2 Theoretical and numerical models**

114 **2.1 Radiation momentum stress tensor method**

115 The ARFs comes from the transfers of linear momentum between the acoustic fields
116 and particles which could be induced by the scattering or absorption. The radiation stress
117 tensor approach^{52,29} is widely employed to compute the static radiation force by
118 integrating the time-averaged radiation stress tensor over a far-field spherical surface S_0 .
119 Consider a particle with arbitrary shape S in an ideal fluid, as shown in Fig. 1, a Bessel
120 beam is incident with arbitrary topological charge and location. Based on the momentum
121 conservation, the radiation stress tensor \mathbf{S}_T in the ideal fluid meets: $\nabla \cdot \langle \mathbf{S}_T \rangle = 0$. By
122 integrating \mathbf{S}_T over the particle surface S , the expression of the ARF could be written

123 as

$$124 \quad \mathbf{F} = -\iint_S \langle \mathbf{S}_T \rangle d\mathbf{S} = -\iint_S \langle L \rangle d\mathbf{S} + \rho_0 \iint_S d\mathbf{S} \cdot \langle \mathbf{u}\mathbf{u} \rangle \quad (1)$$

125 where $\langle L \rangle$ is the time average of the Lagrangian density, ρ_0 is the density of the
 126 surrounding fluid and $\rho_0 \langle \mathbf{u}\mathbf{u} \rangle$ described the average value of the flux of momentum
 127 density tensor. The integral in the ARF expression on the particle surface S could be
 128 transferred to the far-field standard spherical surface S_0 according to the Gaussian
 129 theorem, having

$$130 \quad \mathbf{F} = \iint_{S_0} \langle L \rangle d\mathbf{S} - \rho_0 \iint_{S_0} d\mathbf{S} \cdot \langle \mathbf{u}\mathbf{u} \rangle \quad (2)$$

131 Note that Eq. (2) could apply for the arbitrary-shaped particle since the integral will, in
 132 fact, be conducted in a standard spherical surface, which is very important for both
 133 theoretical and numerical computations. For simplicity, the time average of the
 134 Lagrangian density is divided into three terms: the contribution of only the incident beam
 135 $\langle L_{ii} \rangle$, only the scattered field $\langle L_{ss} \rangle$, and the interaction of the incident and scattered
 136 fields $\langle L_{is} \rangle$, respectively,

$$137 \quad \begin{aligned} \langle L_{ii} \rangle &= \frac{1}{2} \rho_0 \mathbf{u}_i \cdot \mathbf{u}_i - \frac{p_i^2}{2\rho_0 c_0^2} \\ \langle L_{ss} \rangle &= \frac{1}{2} \rho_0 \mathbf{u}_s \cdot \mathbf{u}_s - \frac{p_s^2}{2\rho_0 c_0^2} \\ \langle L_{is} \rangle &= \rho_0 \mathbf{u}_i \cdot \mathbf{u}_s - \frac{p_i p_s}{\rho_0 c_0^2} \end{aligned} \quad (3)$$

138 where c_0 is the velocity in the fluid, $\mathbf{u}_{i,s}$ are the incident and scattered velocity vectors
 139 with $\mathbf{u}_{i,s} = \mathbf{n}u_{i,s}$, \mathbf{n} is the outward unit normal vector, $p_{i,s}$ are the first order pressure
 140 of the incident and scattered fields with the relationship $p_{i,s} = \rho_0 c_0 u_{i,s}$, leading to the

141 vanish of $\langle L_{ss} \rangle$. In addition, there will be no transfer of linear momentum when the
 142 particle does not exist in the fluid, making the terms only related to the incident fields
 143 vanish

$$144 \quad \iint_{S_0} \langle L_{ii} \rangle d\mathbf{S} - \rho_0 \iint_{S_0} d\mathbf{S} \cdot \langle \mathbf{u}_i \mathbf{u}_i \rangle = 0 \quad (4)$$

145 Inserting Eqs. (3) and (4) into (2), the ARF expression in terms of the velocity and
 146 pressure scalar quantities is

$$147 \quad \mathbf{F} = -\iint_{S_0} \left\langle \frac{P_i P_s}{\rho_0 c_0^2} \right\rangle \mathbf{n} dS - \rho_0 \iint_{S_0} \langle u_s u_s \rangle \mathbf{n} dS - \rho_0 \iint_{S_0} \langle u_s u_i \rangle \mathbf{n} dS \quad (5)$$

148 By using the relations between the velocities (pressures) and complex velocity
 149 potentials for both the incident and far-field scattered fields, such as $\mathbf{u}_{i,s} = \nabla \Phi_{i,s}$,
 150 $p_{i,s} = i\omega\rho_0\Phi_{i,s}$ and $u_{i,s} = \mathbf{n} \cdot \nabla \Phi_{i,s} = \partial\Phi_{i,s}/\partial r$ (far-field approximation), the expression of
 151 ARF in terms of velocity potentials could be

$$152 \quad \mathbf{F} = \frac{1}{2} \rho_0 k^2 \iint_{S_0} \text{Re} \left\{ \left(\frac{i}{k} \frac{\partial \Phi_i}{\partial r} - \Phi_i \right) \Phi_s^* - \Phi_s \Phi_s^* \right\} \mathbf{n} dS \quad (6)$$

153 where k is the wave number, * denotes complex conjugation. Φ_i , Φ_s denote the
 154 incident and scattered complex velocity potentials, Re means the real part of a complex
 155 number.

156 From the view of numerical computation, the TMM is an efficient tool to compute
 157 acoustic scattering on nonspherical objects. At present, this method will be further
 158 extended for ARFs which is closely related to the incident and scattered fields. In the
 159 TMM formulation, the velocity potentials of the incident and scattered fields could be

160 expanded as³⁵⁻⁴¹

$$161 \quad \Phi_i = \Phi_0 \sum_{nm} a_{nm} j_n(kr) Y_{nm}(\theta, \varphi) \quad (7)$$

$$162 \quad \Phi_s = \Phi_0 \sum_{nm} s_{nm} h_n^{(1)}(kr) Y_{nm}(\theta, \varphi) \quad (8)$$

163 where a_{nm} and s_{nm} are the incident and scattered coefficients of expansion (others
164 prefer to call the incident and scattered beam-shape coefficients), Φ_0 is the beam
165 amplitude, $j_n(kr)$ and $h_n^{(1)}(kr)$ are the spherical Bessel and Hankel functions of the
166 first kind, respectively. In the far field ($kr \rightarrow \infty$), the following asymptotic expressions of
167 the spherical Bessel function and Hankel function of the first kind are used respectively,
168 as $j_n(kr) \approx i^{-(n+1)} e^{ikr} / 2kr + i^{n+1} e^{-ikr} / 2kr$ and $h_n^{(1)}(kr) \approx i^{-(n+1)} e^{ikr} / kr$. $Y_{nm}(\theta, \varphi)$ denotes
169 the normalized spherical harmonics. The transition relationship between a_{nm} and s_{nm} is
170 given by $s_{nm} = T_{nm, n'm'} a_{n'm'}$, where $T_{nm, n'm'}$ denotes the transition matrix which only
171 depends on the properties of the object, including the geometrical shape, the material
172 composition and the boundary conditions at the interface, and otherwise is independent of
173 the sources. For the exact series solution, the transition matrix could be considered as
174 $T = (s_n - 1) / 2$ without dependence on the azimuthal index m for spheres, which is in
175 fact the partial-wave coefficients a_n with the scattering coefficients s_n known for a
176 wide variety of spheres⁵⁷ and may be taken as a special case for the TMM. Varadan et al.
177 also gave the explicit expressions of the transition matrixes for acoustic soft, hard and
178 fluid sphere⁵⁸, which all coincide with those obtained with the exact series solutions. It is
179 noteworthy that both the TMM³⁵⁻⁴¹ and the series solution for scattering by a sphere can

180 be truncated at appropriate indices (N_{\max}) in computations, which make the asymptotic
 181 expressions of scattered fields convergent in the far-field. After using the far-field
 182 asymptotic expressions for the scattered velocity potentials and implementing several
 183 algebraic manipulations (including the recursion relation of the spherical Bessel function
 184 and its derivative $j_n' = (n/kr)j_n - j_{n+1}$ with the variable kr), the ARF could be given
 185 briefly in terms of the incident and scattered beam shape coefficients, such that

$$186 \quad \mathbf{F} = \frac{1}{2} \rho_0 k^2 \Phi_0^2 \iint_{S_0} \text{Re} \left\{ - \sum_{nm} \sum_{n'm'} \frac{i^{n'-n}}{(kr)^2} (a_{nm} + s_{nm}) s_{n'm'}^* Y_{nm}(\theta, \varphi) Y_{n'm'}^*(\theta, \varphi) \right\} \mathbf{n} dS \quad (9)$$

187 which could be applied for radiation force with arbitrary orientation and agrees with Eqs.
 188 (7) and (9) in Silva's work⁵⁹. The differential surface area is $dS = r^2 \sin \theta d\theta d\varphi$. The
 189 dimensionless ARF \mathbf{Y} is introduced to coincide with the exact solutions for spheres
 190 with the relationship as

$$191 \quad \mathbf{F} = \pi r_0^2 I_0 c_0^{-1} \mathbf{Y} \quad (10)$$

192 where $I_0 = (\rho_0 c_0 / 2) (k \Phi_0)^2$ and r_0 is the characteristic dimension of the target. The
 193 outward unit normal vector is $\mathbf{n} = \sin \theta \cos \varphi \mathbf{e}_x + \sin \theta \sin \varphi \mathbf{e}_y + \cos \theta \mathbf{e}_z$ in Cartesian
 194 ordinates. Hence,

$$195 \quad \mathbf{Y} = - \frac{1}{\pi (kr_0)^2} \iint_{S_0} \text{Re} \left\{ \sum_{nm} \sum_{n'm'} \frac{i^{n'-n}}{(kr)^2} (a_{nm} + s_{nm}) s_{n'm'}^* Y_{nm}(\theta, \varphi) Y_{n'm'}^*(\theta, \varphi) \right\} \quad (11)$$

$$\times (\sin \theta \cos \varphi \mathbf{e}_x + \sin \theta \sin \varphi \mathbf{e}_y + \cos \theta \mathbf{e}_z) r^2 \sin \theta d\theta d\varphi$$

196 The integration could be simplified easily by using Eqs. (15.150-152) in Ref. [60]
 197 for the integration involving the spherical harmonics and circular functions with the

198 detailed derivations given in Appendix A. Finally, the axial and lateral components of the
 199 dimensionless ARFs could be derived independently as

$$200 \quad Y_x = \frac{1}{2\pi(kr_0)^2} \text{Im} \left\{ \sum_{nm} (a_{nm} + s_{nm}) \begin{pmatrix} -s_{n+1,m+1}^* b_{n+1,m} - s_{n-1,m+1}^* b_{n,-m-1} \\ +s_{n+1,m-1}^* b_{n+1,-m} + s_{n-1,m-1}^* b_{n,m-1} \end{pmatrix} \right\} \quad (12)$$

$$201 \quad Y_y = \frac{1}{2\pi(kr_0)^2} \text{Re} \left\{ \sum_{nm} (a_{nm} + s_{nm}) \begin{pmatrix} s_{n+1,m+1}^* b_{n+1,m} + s_{n-1,m+1}^* b_{n,-m-1} \\ +s_{n+1,m-1}^* b_{n+1,-m} + s_{n-1,m-1}^* b_{n,m-1} \end{pmatrix} \right\} \quad (13)$$

$$202 \quad Y_z = \frac{1}{\pi(kr_0)^2} \text{Im} \left\{ \sum_{nm} (a_{nm} + s_{nm}) (s_{n+1,m}^* c_{n+1,m} - s_{n-1,m}^* c_{nm}) \right\} \quad (14)$$

203 where the coefficients are $b_{n,m} = [(n+m)(n+m+1)/(2n-1)(2n+1)]^{1/2}$ and
 204 $c_{n,m} = [(n+m)(n-m)/(2n-1)(2n+1)]^{1/2}$. As observed from Eqs. (12-14), the
 205 three-dimensional ARFs could be obtained once the scattered beam shape coefficients
 206 are calculated from the incident coefficients through various methods, such as the partial
 207 wave series solution, the T-matrix method and other kinds of theoretical and numerical
 208 methods. It is noteworthy that the theoretical expressions of the axial ARF from
 209 spherical shapes in the zeroth- and first-order Bessel beams are derived in Refs. [8-10]
 210 and three-dimensional ARFs for arbitrarily located elastic sphere in Ref. [11].

211 2.2 A brief review of incident beam shape coefficients of arbitrary Bessel beams

212 Consider the Bessel beam is placed in an arbitrary location relative to the particle, as
 213 shown with the coordinate system in Fig. 2. The origin of the $Oxyz$ system O
 214 coincides with the particle centroid, while the origin of the Bessel beam O_B in the
 215 $O_B x' y' z'$ system coordinates is located at (x_0, y_0, z_0) in $Oxyz$. The velocity potential
 216 of a Bessel beam with arbitrary topological charge M and location could be expressed

217 as

$$218 \quad \Phi_B = \Phi_0 i^M e^{ik_z(z-z_0)} J_M(k_r R') e^{iM\varphi'} \quad (15)$$

219 where $R' = \sqrt{(x-x_0)^2 + (y-y_0)^2}$ and $\varphi' = \tan^{-1}[(y-y_0)/(x-x_0)]$ in Fig. 2 describe
 220 the radius and azimuthal angle of the field point (x, y, z) in the $O_B x' y' z'$ system.

221 $k_z = k \cos \beta$ and $k_r = k \sin \beta$ are the axial and transverse component of the wave
 222 number $k = \omega/c_0$ with β the cone angle of the Bessel beam and ω the angular
 223 frequency. By using the addition theorem for the Bessel functions and the exact solution
 224 to the integral on the hybrid product including the associated Legendre, Bessel, and
 225 exponential functions in spherical coordinates as

$$226 \quad \int_{\theta=0}^{\pi} d\theta \sin \theta e^{ikr \cos \beta \cos \theta} P_n^m(\cos \theta) J_m(kr \sin \beta \sin \theta) = 2i^{n-m} P_n^m(\cos \beta) j_n(kr) \quad (16)$$

227 The incident beam shape coefficients of the Bessel beam with arbitrary topological
 228 charge and location could be derived³⁵

$$229 \quad a_{nm} = 4\pi \xi_{nm} i^{n-m+M} P_n^m(\cos \beta) \times e^{-ik_z z_0} J_{m-M}(\sigma_0) e^{-i(m-M)\varphi_0} \quad (17)$$

230 with the normalized coefficients $\xi_{nm} = [(2n+1)(n-m)!]^{1/2} [4\pi(n+m)!]^{-1/2}$, $\sigma_0 = k_r R_0$,

231 $R_0 = (x_0^2 + y_0^2)^{1/2}$ and $\varphi_0 = \tan^{-1}(y_0/x_0)$. When the offset is $(x_0, y_0, z_0) = (0, 0, 0)$, Eq.

232 (17) will degenerate into the on-axis incidence situation of the Bessel beam.

233 The scattered beam shape coefficients s_{nm} are still missing to calculate the
 234 three-dimensional ARFs based on Eqs. (12-14). In this work, a versatile TMM (which
 235 gives a linear relationship between the incident and scattered beam shape coefficients as

236 $s_{nm} = T_{nm, n'm'} a_{n'm'}$) is introduced to the field of radiation forces. Note that the TMM in the

237 acoustic field mainly considers the scattering field in underwater or elastic mediums
238 instead of the further consideration on the acoustic radiation forces and torques. The
239 present work is inspired to take advantage of this method (as discussed in the
240 Introduction) which is very efficient for both spherical and aspherical shapes with
241 rotational symmetry and only needs to be computed once for the transition (T) matrix as
242 shown in the Appendix B. The TMM makes it possible to employ nonspherical shapes to
243 model the real interesting particles in life science and engineering in an exacter manner.

244 **3 Numerical results and discussion**

245 **3.1 Validation of T-matrix method for acoustic radiation force**

246 To verify the correctness of the TMM, several examples are implemented for a rigid
247 sphere in the ordinary (OBB, blue dashed line) and first-order helicoidal Bessel beams
248 (FHBB, red solid line) as shown in Fig. 3(a). Both cases are under on-axis incidence. The
249 axial ARFs Y_z for the OBB case are extracted from Fig. 2 of Ref. [8] with the half-cone
250 angle $\beta = 60^\circ$ [blue circles in Fig. 3(a)], while those for the HBB are extracted from Fig.
251 1 of Ref. [10] with $\beta = 66.42^\circ$ [red triangles in Fig.3(a)]. The reference results are
252 calculated with the exact series solutions (partial-wave series method). As shown in Fig.
253 3(a), all the TMM results agree well with the series solutions. In addition, the axial ARFs
254 Y_z for a rigid sphere located off the OBB axis have been calculated by TMM and
255 partial-wave series method based on the multipole expansion method, with the references

256 given by the boundary element method (Fig. 11 in Ref. [46]). The cone angle is $\beta=30^\circ$,
257 dimensionless frequency $ka=1$, and x_0 describes the offset with the length unit in
258 meters. As shown in Fig. 3(b), the results from the TMM and partial-wave series coincide
259 with each other and agree well with those from the Boundary element method. Moreover,
260 the TMM has been demonstrated for the scattering from spheroid³⁶⁻³⁹, finite cylinder^{40,41}
261 in plane wave and Bessel beams, and hence it could be applied for the radiation forces for
262 these shapes convincingly provided that the incident and scattered coefficients of
263 expansion are computed correctly [see Eqs. (12-14)]. It is noteworthy that the incident
264 and scattered coefficients (occurring as column vectors in our numerical computations
265 with the TMM) will be assembled in the same way for the radiation force. This will
266 further verify the effectiveness of the present derivation of the ARF using the TMM and
267 the corresponding homemade codes.

268 Furthermore, the convergence curves of the TMM are discussed in terms of the axial
269 ARF versus different truncation number N_{\max} for a biconcave shape [see Fig. 3(c) for
270 the 2D schematic, taking the "peanut-shaped" generalized superspheroid as an example].
271 The definitions of a and b for the generalized superspheroid in Fig. 3(c) are
272 analogous with those for a spheroid³⁶. For the rotational symmetry of the generalized
273 superspheroid, the distance of the surface field to the origin (center of the object) could
274 be expressed as $r_s(\theta)=(a^2 \cos^2 \theta + b^2 \sin^2 \theta)^{1/2}$, where θ is the polar angle of the
275 surface field point, which are used by implementing an integral over the object surface to

276 obtain the transition matrix $T_{mm,n'm'}$ relating the incident coefficients to the scattered
 277 coefficients of expansion. Note that due to the rotational symmetry, the integral involving
 278 the term $r_s(\theta)$ over the surface is only dependent on the polar angle, otherwise
 279 independent of the azimuthal angle. Fig. 3(d) depicts the axial ARFs of a rigid
 280 "peanut-shaped" generalized superspheroid with the aspect ratio $a/b = 4$. The incident
 281 wave is a first-order Bessel beam with an arbitrary cone angle (here we choose
 282 $\beta = 66.42^\circ$) and the dimensionless frequency $kr_0 = 8$ where r_0 is the characteristic
 283 length of the nonspherical object. Under this circumstance, r_0 is the larger value
 284 between a and b . The on-axis incidence is described by the blue solid line with
 285 triangles, while the off-axis case with the offset $(x_0, y_0) = (0.1\pi/kr_0, 0.1\pi/kr_0)$ is
 286 described by the red solid line with circles. (x_0, y_0) are the translational coordinates of
 287 the beam center with respect to that of the object (i.e. the origin of the considered
 288 coordinates). A convergence test for a rigid finite cylinder with spherical endcaps has
 289 been conducted in Ref. [40] and hence omitted for brevity. All these curves converge
 290 very fast versus N_{\max} , which further demonstrates the efficiency of the present TMM for
 291 ARF. In the following computations, the truncation number is set as
 292 $N_{\max} = 2 + \text{Int}\left(8 + kr_0 + 4.05\sqrt[3]{kr_0}\right)$, which could ensure the accuracy and convergence of
 293 the present computations according to our tests. The symbol Int means to round the
 294 following number towards the positive infinity. Both the accuracy and convergence tests
 295 and related discussions provide enough validation of the T-matrix method for acoustic

296 radiation force.

297 **3.2 Axial ARF reversal and physical mechanism**

298 Two numerical experiments were conducted with the emphasis on the negative
299 ARFs exerted on the rigid oblate and prolate spheroids in Bessel beams and the related
300 physical mechanisms. The Neumann boundary condition was applied throughout for
301 objects including spheroids, generalized superspheroids and finite cylinders in the
302 following. In this Section, the rotational axis of the rigid spheroid coincides with the
303 incident beam axis. Note that the relative orientation of the spheroid to the beam axis
304 changes the scattering field from the particle, leading to the alteration of the transfer of
305 linear momentum from the incident acoustic beam to the particle. The Y_z of the oblate
306 and prolate spheroids versus the dimensionless frequency kr_0 in the FHBB are depicted
307 in **Fig. 4(a)** for $a/b=1/2$ and **Fig. 4(b)** for $a/b=2$, with $\beta=30^\circ$, 66.42° , and 80° .
308 a is the polar radius and b is the equatorial radius.²⁹ The ranges including the negative
309 ARFs in panels (a) and (b) are zoomed in and presented in panels (c) and (d) of **Fig. 4**,
310 respectively. It implies that a large β (sufficiently nonparaxial) may facilitate the
311 pulling force since the negative ARFs appear for both cases with $\beta=80^\circ$ in the
312 considered region, while it fails for $\beta=30^\circ$. Especially, negative ARF is impossible for
313 plane waves ($\beta=0^\circ$) with passive spheres^{19,61}. The term in Eq. (21) of **Ref. [19]**
314 ($F_z = P_{sca} c^{-1} (\cos \beta - \langle \cos \theta_s \rangle)$ without absorption) including $\cos \beta$ represents the
315 momentum removed from the incident Bessel beam (which induces positive ARF) and

316 the term including $-\langle \cos \theta_s \rangle$ gives the axial projection of the momentum transport
 317 associated with the scattered field (which may induce positive or negative ARF), where
 318 θ_s is the polar angle of the field point with respect to the positive z -direction [see Fig.
 319 3(c)]. The schematic of Fig. 1 qualitatively describes how to produce a negative ARF on
 320 an arbitrary object. The red solid arrows in the forward hemisphere denote the total
 321 scattered fields with the forward axial components, while the blue dashed arrows in the
 322 backward hemisphere represent the total scattered field with the backward axial
 323 components. The resultant forward component of all the scattering denoted by the red
 324 solid arrows are relatively larger than the resultant backward component of all scattering
 325 denoted by the blue dashed arrows. To further reveal the physical mechanism
 326 quantitatively, the angular dependences of the scattered form functions versus the
 327 scattered polar angle θ_s for the oblate spheroid in the FHBB with $\beta=80^\circ$ are plotted in
 328 Fig. 4(e) with $kr_0=1.8$ [marked as the red pentagram in Fig. 4(c)] and $kr_0=2.1$
 329 [marked as the blue pentagram in Fig. 4(c)]. The black dotted line denotes the direction of
 330 the incident wave vector (i.e. $\theta_s=\beta$). As shown in the enlarged view in Fig. 4(c), the
 331 ARF is negative at $kr_0=1.8$, and otherwise positive at $kr_0=2.1$. It can be observed in
 332 Fig. 4(e) that for $kr_0=1.8$, the scattering dominates in the forward directions with
 333 $\theta_s < \beta$, resulting in the negative ARF; for $kr_0=2.1$, the scattering in the backward is
 334 relatively stronger than that in the forward, leading to the positive ARF. To better
 335 understand the relationship between the axial ARFs and two-dimensional scattering

336 patterns, the scattering patterns of form functions for both the oblate and prolate
337 spheroids in the first-order HBB ($M=1$) with cone angle $\beta=80^\circ$ are given versus
338 different dimensionless frequencies ranging from $kr_0=10$ to $kr_0=0.2$ [See Mov1 in
339 Supplemental Material at [URL](#)]. Note that at high frequencies, the forward scattering is
340 comparable with the scattering in the backward hemisphere, however, the positive axial
341 force induced by the incident wave ($P_{sca} c^{-1} \cos \beta$) is important and lead to the resultant
342 axial force positive.

343 3.3 Pulling forces on typical nonspherical objects

344 After giving an explicit explanation of the physical mechanism for the negative ARF,
345 the emphasis will be put on the parameter conditions for exerting the pulling force on
346 several typical objects, which may have potential applications in acoustophoresis, surface
347 chemistry, atomic physics, ultrasonic medicine, reduced gravity environment, and so on.
348 Panels (a-d) of Fig.5 study the influence of the topological charges (orders) of the Bessel
349 beams for a "peanut-shaped" generalized superspheroid with $a/b=2$ for an on-axis
350 incidence. The 2D plots depict the negative ARF "islands" in the (kr_0, β) domain and
351 the white domains stand for the positive ARFs (not shown numerically). The islands of
352 the negative ARF are different between the OBB and HBBs since panel (a) has two
353 subregions, while panels (b-d) have one subregion under consideration. For the HBBs,
354 the frequencies of the negative ARF seem to increase with the increase of the beam order.
355 To discuss the parameter of the aspect ratio, the 2D plots of a generalized superspheroid

356 with $a/b=3$ and $a/b=4$ in the FHBB are given in panel (e) and (f) [compared with
357 panel (b)], respectively. These results imply that the distributions of the negative ARF
358 depend on both the beams and objects. However, the central frequencies do not change
359 greatly with the aspect ratios. The oblate case for the generalized superspheroid is also
360 described in panel (g). This shape is like some biological cells, the red blood cell with a
361 dip in the center for example. In biomedicine or reduced gravity environment, the finite
362 cylinder shapes with endcaps are helpful to model several kinds of bacteria or space
363 shuttle, which will be discussed as follows. Capsule-shaped (cylinder with spherical
364 endcaps^{40,41}) objects are investigated for both the on-axis [panel (h)] and off-axis
365 incidences [panels (i-l)]. The aspect ratio is $l/b=2$ for all the cases, where l is the half
366 length of the total cylinder and b is the radius of the cylindrical portion.⁴⁰ Panels (h-j)
367 are for FHBB while Panels (k,l) are for SHBB. The beam axis is shifted off the axis of
368 the object in the transverse plane as $(0.1\pi/kr_0, 0.1\pi/kr_0)$ for Fig. 5(i,k) and
369 $(0.5\pi/kr_0, 0.5\pi/kr_0)$ for Fig. 5(j, l). Note that there is no need for the extra
370 computational cost for the off-axis incidence compared with the on-axis case³⁵. By
371 comparison, the area of the negative force island decreases with a larger offset with
372 respect to the object's center for both the FHBB and SHBB. It also implies that the
373 negative ARFs occur at higher frequencies with a larger offset by comparing Fig.5(i) with
374 Fig.5(j) [or Fig.5(k) with Fig.5(l)]. Unfortunately, quantitative results for the orientation
375 dependence of the negative force are not available although it is known that to induce a

376 negative axial ARF the scattering in the forward hemisphere needs to be stronger than
377 scattering in the backward hemisphere²⁹.

378 One of the most important results concerns the extent of the first-order HBB
379 negative ARF regions in evident in Fig. 5 (b) and (h) where the cone angle β can be as
380 small as 54 degrees. For fixed rigid spheres on the axis of a first-order HBB it has long
381 been known that conditions can be found giving negative axial ARF^{8,10}. The smallest
382 value of β for a first-order HBB to produce negative ARF on a rigid sphere is known to
383 be β of approximately 63 degrees. Inspection of Fig. 5 (b) and (h) shows that for an
384 appropriately elongated generalized superspheroid [Fig. 5(b)] and capsule [Fig. 5(h)] the
385 associated values can be as small as 54 and 55 degrees, respectively. This suggests those
386 shapes of elongated objects can be especially favorable for producing negative axial ARF
387 in first-order HBB.

388 **3.4 Three dimensional ARFs for typical nonspherical objects**

389 The three-dimensional ARFs (from the first to third column) of typical concave and
390 convex shapes are investigated versus the dimensionless frequencies kr_0 , the cone angle
391 of the Bessel beam β and the transverse offset (x_0, y_0) , as shown in Fig. 6. The
392 first-order HBB is considered with both on- (first row) and off-axis incidences (second
393 and third rows). The offset is set as $(x_0, y_0) = (0.5\pi/kr_0, 0.5\pi/kr_0)$. The generalized
394 superspheroid with $a/b = 2$ (first and second rows) is discussed at first and it could be
395 found that the transverse ARFs vanish for the on-axis incidence because of the rotational

396 symmetry of both the incident Bessel beam and geometric shape. However, for the
397 off-axis incidence, the transverse ARFs will exist, see Fig. 6(d) and 6(e). To investigate
398 the effect of the geometric shapes on the three-dimensional ARFs, the ARFs of a
399 smoothed spheroid with the same aspect ratio $a/b = 2$ and offset are given in the third
400 row of Fig. 6. By comparison of the ARFs in the second and third rows, the main profiles
401 of ARFs in the two-dimensional (kr_0, β) regions are similar for the same aspect ratio
402 and off-set. However, there are some “jumps” in the ARFs patterns versus (kr_0, β) at
403 relatively high frequencies (e.g., $kr_0 \geq 4.75$). This is due to the fact that the scattering
404 patterns will be more easily influenced when the aspect of the geometric shape
405 comparable with the wavelength (i.e., relatively high frequency), which is further
406 demonstrated by the similar ARFs patterns at low frequencies, see the second and third
407 rows.

408 In addition, the three-dimensional ARFs of the generalized superspheroid with
409 $a/b = 2$ are studied versus the offset x_0 and y_0 in ordinary (order=0), first-order
410 (order=1) and second- order (order=2) Bessel beams, as depicted in Fig. 7. The range of
411 the offset is $-1 \leq x_0 \leq 1$ and $-1 \leq y_0 \leq 1$, with the increase are $\Delta x_0 (\Delta y_0) = 0.02$. The
412 incident dimensionless frequency is $kr_0 = 10$ and cone angle $\beta = 30^\circ$. As observed in
413 the first (Y_x) and second (Y_y) columns, the transverse ARFs versus the offsets (x_0, y_0)
414 have the rotational symmetry with the angle of $\pi/2$. This could be easily understood by
415 the reciprocity of transverse ARFs in x and y directions. Furthermore, the axial ARFs

416 of OBB and HBBs are different such that the maximum value occurs at the axis for the
417 OBB while at the concentric ring for the HBBs, which depends on the structure profiles
418 of the Bessel beams. The three-dimensional ARFs could be used to discuss the trapping
419 stability and the dynamic motions (axial translocation and orbital rotation around the
420 beam axis) of particles in the Bessel beams. To further understand the three-dimensional
421 ARFs of the generalized superspheroid versus different dimensional frequencies and
422 transverse offsets, the ARFs are given when the superspheroid is placed in the ordinary
423 ($M=0$), first-order ($M=1$), and second-order ($M=2$) Bessel beams, respectively, with a
424 fixed cone angle $\beta = 30^\circ$ and the frequencies ranging from $kr_0=0.2$ to $kr_0=10$ [see
425 Mov2 in Supplemental Material at [URL](#)]. The transverse forces are given in the form of
426 arrow patterns, while the axial force is placed in the background with the colormaps.

427 3.5 Axial ARFs of rigid spheres in Standing Bessel Waves

428 The incident beam shape coefficients of a traveling Bessel beam are given
429 theoretically in Eq. (17)³⁵, which could be easily extended for the standing Bessel waves.

430 The velocity potential Φ_{SB} of a standing Bessel beams could be written as

$$431 \quad \Phi_{SB} = \Phi_0 i^M \left[A e^{ik_z(z-z_0+h)} + B e^{-ik_z(z-z_0+h)} \right] \times J_M(k_r R') e^{iM\varphi'} \quad (18)$$

432 where h is the axial distance between the particle centroid and nearest pressure antinode,

433 A and B are the amplitudes of the two beams with opposite propagation. To keep the

434 energy of the standing fields the same as the traveling Bessel beam, one has $A^2 + B^2 = 1$,

435 with $B = \alpha A$ and $A = 1/\sqrt{1+\alpha^2}$. Conducting the similar derivation of the beam shape

436 coefficients of a single Bessel beam, the theoretical derivations for the standing Bessel
437 beams could be de obtained as

$$438 \quad a_{nm} = 4\pi\xi_{nm} \left[A e^{ik_z(-z_0+h)} + B e^{-ik_z(-z_0+h)} (-1)^{n-m} \right] i^{n-m+M} P_n^m(\cos\beta) J_{m-M}(\sigma_0) e^{-i(m-M)\phi_0} \quad (19)$$

439 Both the axial ARFs of a rigid sphere in a standing ($\alpha = 1$) and traveling ($\alpha = 0$)
440 Bessel beams with different orders (order=0, 1, 2, and 3) are calculated versus the
441 dimensional frequency ka with a fixed cone angle $\beta = 60^\circ$. As observed in Fig. 8,
442 axial force curves in standing Bessel waves show intuitive oscillation characteristics
443 versus the dimensionless frequency as similar to the plane standing waves, which are
444 different from those in traveling Bessel beams. However, the fabrication set-ups for
445 Bessel beams and calibration of two counter-propagating Bessel beams will be
446 challenging in experimental and applied investigations.

447 **4 Conclusions**

448 Computation of three-dimensional acoustic radiation forces on objects with complex
449 geometrical shapes and boundary conditions is a challenging topic in engineering
450 applications. Previous derivations of the acoustic radiation pressure are based on the long
451 wavelength approximation⁶²⁻⁶⁴ which has the limitation that the particle size is much
452 smaller than the acoustic wavelength. Recently, the partial wave series solution has been
453 introduced to study the ARF in the context of a Bessel beam without the limitation of
454 computational frequencies. However, this exact solution may be restricted to certain
455 shapes⁸⁻¹⁰. The T-matrix method is quite helpful for typical objects in engineering and

456 especially efficient for shapes with rotational symmetry. In addition, the TMM could be
457 employed for scattering problems involved in a waveguide⁶⁵ or multiple scattering⁶⁶
458 (including objects of multilayers and/or arbitrary numbers), which could be further
459 extended for the ARFs based on the present work. The present numerical experiments
460 demonstrate the effectiveness of the TMM to calculate the ARFs for several typical
461 shapes, and the negative axial ARFs are obtained under certain conditions with the
462 corresponding physical mechanisms. The TMM is very versatile for both spherical and
463 nonspherical shapes with different material composition^{34-41,58} once the geometrical shape
464 functions could be given explicitly, providing an alternative to theoretical and
465 experimental approaches. Other numerical methods, such as the finite volume method
466 (FVM)^{47,48}, the (modified) finite element method (FEM)^{68,69}, the boundary element
467 method (BEM)⁴⁴⁻⁴⁶, the finite-difference time-domain method (FDTD)⁵¹, and methods
468 based on the ray acoustics approach⁶⁹ and the perturbation theory⁷⁰, may combine with
469 the present derivation to provide more choices for the computations of ARF in Bessel
470 beams. The TMM can be also used to calculate the acoustic radiation torques⁷¹, which has
471 been implemented in optics with the TMM⁷² for a Gaussian beam incidence⁷³ by using
472 the sums of products of the expansion coefficients for the integrals of the angular
473 momentum fluxes⁷⁴. The design of the acoustic tweezers numerical toolbox will benefit
474 from the present work as similar to that in Optics⁷³. It is anticipated that the
475 three-dimensional ARFs could be obtained immediately once the scattered coefficients

476 could be calculated according to a certain incident wave. The dynamic motions could be
477 obtained for the axial translocation and orbital rotation around the beam axis. The long
478 nonspherical shape may be especially favorable for producing negative axial ARF in
479 Bessel beams, which is potential in the fields of microfluidics and life sciences. A brief
480 theoretical derivation of the beam shape coefficients for the standing Bessel beams is
481 given with the comparisons of axial ARFs in both standing and traveling beams, which
482 may provide more possibility for the particle manipulations with vortex beams.

483

484 Appendix:

485 A. Detailed derivations of Three-dimensional ARFs

486

487 To conduct the integrals of products including spherical harmonics and
488 trigonometric functions over the solid angle in Eq. (11), the following formulas should be
489 introduced based on the Eqs. (15.150-152) in Ref. [60] for the three-dimensional
490 dimensionless ARFs Y_x , Y_y and Y_z , respectively

$$\begin{aligned} & \int_0^{2\pi} \int_0^\pi Y_{nm}(\theta, \varphi) Y_{n'm'}^*(\theta, \varphi) \sin^2 \theta \cos \varphi d\theta d\varphi \\ 491 & = -\frac{1}{2} (b_{n+1,m} \delta_{m',m+1} \delta_{n',n+1} - b_{n,-m-1} \delta_{m',m+1} \delta_{n',n-1} - b_{n+1,-m} \delta_{m',m-1} \delta_{n',n+1} + b_{n,m-1} \delta_{m',m-1} \delta_{n',n-1}); \end{aligned} \quad (\text{A1})$$

$$\begin{aligned} & \int_0^{2\pi} \int_0^\pi Y_{nm}(\theta, \varphi) Y_{n'm'}^*(\theta, \varphi) \sin^2 \theta \sin \varphi d\theta d\varphi \\ 492 & = \frac{i}{2} (b_{n+1,m} \delta_{m',m+1} \delta_{n',n+1} - b_{n,-m-1} \delta_{m',m+1} \delta_{n',n-1} + b_{n+1,-m} \delta_{m',m-1} \delta_{n',n+1} - b_{n,m-1} \delta_{m',m-1} \delta_{n',n-1}); \end{aligned} \quad (\text{A2})$$

$$493 \int_0^{2\pi} \int_0^\pi Y_{nm}(\theta, \varphi) Y_{n'm'}^*(\theta, \varphi) \sin \theta \cos \theta d\theta d\varphi = (c_{n+1,m} \delta_{m',m} \delta_{n',n+1} + c_{n,m} \delta_{m',m} \delta_{n',n-1}); \quad (\text{A3})$$

494 where δ is the Kronecker delta function. Substituting Eqs. (A1)-(A3) into the three
495 components into Eq. (11), the explicit expressions are obtained as Eqs. (12-14) with the
496 corresponding coefficients therein.

497 B. Explicit expression of transition (T) matrix

498 The incident and scattered beam shape coefficients are related by the transition
499 matrix, depending on the geometric shape, material composition, and boundary
500 conditions at the interface of the particle. For a rigid particle with rotational symmetry,

501 the T matrix could be calculated as $\mathbf{T} = -\text{Re}\mathbf{Q}\mathbf{Q}^{-1}$ with the element of the \mathbf{Q} matrix
 502 derived as³⁶

$$503 \quad Q_{nm,n'm'}^{\sigma\sigma'} = \int_0^\pi \xi_{n'm'} J_{n'}(kr) P_{n'}^{m'}(\cos\theta) \xi_{nm} \left[\frac{\partial h_n^{(1)}(kr)}{\partial r} P_n^m(\cos\theta) - \frac{r_\theta}{r^2} h_n^{(1)}(kr) \frac{\partial P_n^m(\cos\theta)}{\partial \theta} \right] \times r^2 \sin\theta d\theta \int_0^{2\pi} \begin{pmatrix} \cos m'\varphi \\ \sin m'\varphi \end{pmatrix} \begin{pmatrix} \cos m\varphi \\ \sin m\varphi \end{pmatrix} d\varphi \quad (\text{A4})$$

504 where $r(\theta)$ is the geometric shape function and $r_\theta = dr/d\theta$ is the derivate of $r(\theta)$
 505 with respect to the polar angle θ on the particle surface. Further details and simplified
 506 methods could be found in Refs. [36,40]. In fact, the \mathbf{Q} matrix could be calculated for
 507 an arbitrary shape from the point of view of theory, however, there can be severe
 508 numerical difficulties in the general situation. The TMM is quite efficient for rotational
 509 shapes as demonstrated in the literature over the past decades.

510

511 **References**

- 512 1. J. Wu, *J. Acoust. Soc. Am.*, **89**, 2140 (1991).
- 513 2. H. Bruus, J. Dual, J. Hawkes, M. Hill, T. Laurell, J. Nilsson, S. Radel, S. Sadhal and M.
- 514 Wiklundh, *Lab Chip*, **11**, 3579 (2011).
- 515 3. J.-L. Thomas, R. Marchiano and D. Baresch, *J. Quant. Spectrosc. Radiat. Transf.*, **195**,
- 516 55 (2017).
- 517 4. A. Ozcelik, J. Rufo, F. Guo, Y. Gu, P. Li, J. Lata and T. J. Huang, *Nature Methods*, **15**,
- 518 1021 (2018).
- 519 5. A. Ashkin, J. M. Dziedzic, J. E. Bjorkholm and S. Chu, *Opt. let.*, **11**, 288 (1986).
- 520 6. R. E. Apfel, *J. Acoust. Soc. Am.*, **70**, 636 (1981).
- 521 7. D. Foresti, M. Nabavi and D. Poulikakos, *J. Fluid Mech.*, **709**, 581 (2012).
- 522 8. P. L. Marston, *J. Acoust. Soc. Am.*, **120**, 3518 (2006).
- 523 9. P. L. Marston, *J. Acoust. Soc. Am.*, **122**, 3162 (2007).
- 524 10. P. L. Marston, *J. Acoust. Soc. Am.*, **125**, 3539 (2009).
- 525 11. D. Baresch, J.-L. Thomas and R. Marchiano, *J. Acoust. Soc. Am.*, **133**, 25 (2013).
- 526 12. C. E. M. Démoré, P. M. Dahl, Z. Yang, P. Glynne-Jones, A. Melzer, S. Cochran, M.
- 527 P. MacDonald and G. C. Spalding, *Phys. Rev. Lett.*, **112**, 174302 (2014).
- 528 13. X.-D Fan and L. Zhang, *Phys. Rev. Applied*, **11**, 014055 (2019).
- 529 14. C. R. P. Courtney, C. E. M. Demore, H. Wu, A. Grinenko, P. D. Wilcox, S. Cochran
- 530 and B. W. Drinkwater, *Appl. Phys. Lett.*, **104**, 154103 (2014).

- 531 15. B. W. Drinkwater, *Lab Chip*, **16**, 2360 (2016).
- 532 16. A. Marzo and B. W. Drinkwater, *Proc. Natl. Acad. Sci. U.S.A.*, **116**, 84 (2019).
- 533 17. D. Baresch, J.-L. Thomas and R. Marchiano, *Phys. Rev. Lett.*, **116**, 024301 (2016).
- 534 18. J. Chen, J. Ng, Z. Lin and C. T. Chan, *Nat. Photonics*, **5**, 531 (2011).
- 535 19. L. Zhang and P. L. Marston, *Phys. Rev. E*, **84**, 035601 (2011).
- 536 20. A. Novitsky, C. W. Qiu and H. Wang, *Phys. Rev. Lett.*, **107**, 203601 (2011).
- 537 21. G. T. Silva and A. L. Baggio, *Ultrasonics*, **56**, 449-455 (2015).
- 538 22. X. Jiang, Y. Li, B. Liang, J.-C. Cheng and L. Zhang, *Phys. Rev. Lett.*, **117**, 034301
- 539 (2016).
- 540 23. B. T. Hefner and P. L. Marston, *J. Acoust. Soc. Am.*, **106**, 3313 (1999).
- 541 24. A. Riaud, J.-L. Thomas, E. Charron, A. Bussonnière, O. B. Matar and M. Baudoin,
- 542 *Phys. Rev. Applied*, **4**, 034004 (2015).
- 543 25. A. Riaud, M. Baudoin, O. B. Matar, L. Becerra and J.-L. Thomas, *Phys. Rev. Applied*,
- 544 **7**, 024007 (2017).
- 545 26. M. Baudoin, J.-C. Gerbedoen, A. Riaud, O. B. Matar, N. Smagin and J.-L. Thomas,
- 546 *Sci. Adv.*, **5**, eaav1967 (2019).
- 547 27. N. Jiménez, R. Picó, V. Sánchez-Morcillo, V. Romero-García, L. M. García-Raffi and
- 548 K. Staliunas, *Phys. Rev. E*, **94**, 053004 (2016).
- 549 28. K. Tang, Y. Hong, C. Qiu, S. Peng, M. Ke, Z. Liu, *Jpn. J. Appl. Phys.*, **55**, 110302
- 550 (2016).

- 551 29. L. Zhang and P. L. Marston, *J. Acoust. Soc. Am.*, **131**, EL329 (2012).
- 552 30. L. Zhang and P. L. Marston, *Biomed. Opt. Express*, **4**, 1610 (2013); Erratum, **4**, 2988
553 (2013).
- 554 31. F. G. Mitri and G. T. Silva, *Phys. Rev. E*, **90**, 053204 (2014).
- 555 32. P. L. Marston, *J. Acoust. Soc. Am.*, **135**, 1668 (2014).
- 556 33. L. Zhang, *J. Acoust. Soc. Am.*, **145**, EL185 (2019).
- 557 34. V. V. Varadan, A. Lakhtakia and V. K. Varadan, *J. Acoust. Soc. Am.*, **84**, 2280
558 (1988).
- 559 35. Z. Gong, P. L. Marston, W. Li and Y. Chai, *J. Acoust. Soc. Am.*, **141**, EL574 (2017).
- 560 36. Z. Gong, W. Li, F. G. Mitri, Y. Chai and Y. Zhao, *J. Sound Vibr.*, **383**, 233 (2016).
- 561 37. P. C. Waterman, *J. Acoust. Soc. Am.*, **125**, 42 (2009).
- 562 38. R. Lim, *J. Acoust. Soc. Am.*, **138**, 2266 (2015).
- 563 39. R. Lim, *J. Acoust. Soc. Am.*, **142**, 1362 (2017).
- 564 40. Z. Gong, W. Li, Y. Chai, Y. Zhao and & F. G. Mitri, *Ocean Eng.*, **129**, 507 (2017).
- 565 41. W. Li, Y. Chai, Z. Gong and P. L. Marston, *J. Quant. Spectrosc. Radiat. Transf.*, **200**,
566 146 (2017).
- 567 42. A. Neild, S. Oberti, A. Haake and J. Dual, *Ultrasonics*, **44**, e455 (2006).
- 568 43. P. B. Muller, R. Barnkob, M. J. H. Jensen and H. Bruus, *Lab Chip*, **12**, 4617 (2012).
- 569 44. W. J. Xie and B. Wei, *Appl. Phys. Lett.*, **79**, 881 (2001).
- 570 45. F. B. Wijaya and K. M. Lim, *Acta Acust. United Acust.*, **101**, 531 (2015).

571 46. F. B. Wijaya and K. M. Lim, *Proceedings of Meetings on Acoustics 171ASA*, **26**,
572 045002 (2016).

573 47. J. Wang and J. Dual, *J. Phys. A: Math. Theor.*, **42**, 285502 (2009).

574 48. J. Dual, P. Hahn, I. Leibacher, D. Moller, T. Schwarz and J. Wang, *Lab Chip*, **12**,
575 4010 (2012).

576 49. D. Haydock, *J. Phys. A: Math. Gen.*, **38**, 3265 (2005).

577 50. G. Barrios and R. Rechtman, *J. Fluid Mech.*, **596**, 191 (2008).

578 51. F. Cai, L. Meng, C. Jiang, Y. Pan and H. Zheng, *J. Acoust. Soc. Am.*, **128**, 1617
579 (2010).

580 52. P. J. Westervelt, *J. Acoust. Soc. Am.*, **29**, 26 (1957).

581 53. L. Zhang *J. Acoust. Soc. Am.*, **143**, 2796 (2018).

582 54. G. T. Silva, J. H. Lopes and F. G. Mitri, *IEEE Trans. Ultrason. Ferroelectr. Freq.*
583 *Control*, **60**, 1207 (2013).

584 55. P. L. Marston, W. Wei and D. B. Thiessen, *AIP Conference Proceedings*, **838**, 495
585 (2006).

586 56. G. T. Silva and B. W. Drinkwater, *J. Acoust. Soc. Am.*, **144**, EL453 (2018).

587 57. P. L. Marston, *J. Acoust. Soc. Am.*, **121**, 753 (2007).

588 58. V.V. Varadan, A. Lakhtakia and V. K. Varadan, *Field representations and*
589 *introduction to scattering*, Secs. 5.5, pp. 238-239 (Elsevier Science Publishers,
590 North-Holland, 1991).

- 591 59. G. T. Silva, *J. Acoust. Soc. Am.*, **130**, 3541 (2011).
- 592 60. G. B. Arfken, H. J. Weber and F. E. Harris, *Mathematical Methods for Physicists*, 7th
593 Ed., Sec. 15.5, pp.764 (Elsevier, New York, 2013).
- 594 61. P. L. Marston and L. Zhang, *J. Acoust. Soc. Am.*, **139**, 3139 (2016).
- 595 62. L. V. King, *Proc.R. Soc. London, Ser. A*, **147**, 212 (1934).
- 596 63. K. Yosioka and Y. Kawasima, *Acustica*, **5**, 167 (1955).
- 597 64. L. P. Gor'Kov, *Sov. Phys. Dokl.*, **6**, 773 (1962).
- 598 65. A. Boström, *Wave motion*, **2**, 167 (1980).
- 599 66. A. Boström, *J. Acoust. Soc. Am.*, **67**, 399 (1980).
- 600 67. Z. Gong, Y. Chai and W. Li, *Int. J. Comput. Methods*, **13**, 1640007 (2016).
- 601 68. Y. Chai, W. Li, Z. Gong and T. Li, *Ocean Eng.*, **116**, 129 (2016).
- 602 69. J. Lee and K. K. Shung, *J. Acoust. Soc. Am.*, **120**, 1084 (2006).
- 603 70. H. Bruus, *Lab Chip*, **12**, 1014 (2012).
- 604 71. Z. Gong, P. L. Marston and W. Li, *Phys. Rev. Applied*, In production (2019).
- 605 72. M. I. Mishchenko, L. D. Travis and A. A. Lacis, *Scattering, Absorption, and*
606 *Emission of Light by Small Particles*, Secs. 5.1-5.2, 5.11-5.13, pp. 115-127, 165-189
607 (Cambridge University Press, Cambridge, 2002).
- 608 73. T. A. Nieminen, V. L. Y. Loke, A. B. Stilgoe, G. Knoner, A. M. Branczyk, N. R.
609 Heckenberg and H. Rubinsztein-Dunlop, *J. Opt. A: Pure Appl. Opt.*, **9**, S196 (2007).
- 610 74. J. H. Crichton and P. L. Marston, *Electron. J. Differ. Equ.*, **4**, 37 (2000).

612 **Acknowledgments**

613 Work supported by HUST Postgraduate Overseas Short-term Study Program Scholarship

614 and China Scholarship Council (Z.G.), NSFC (W.L. and Z.G.) and ONR (P.L.M).

615

616 **Figure captions**

617 **Fig. 1** (Color online) Schematic of an arbitrary 3D object in an ideal fluid illuminated by
618 a helicoidal Bessel beam (HBB) with arbitrary order and location. The acoustic scattering
619 in the forward half-space (red solid arrows) is relatively stronger than the scattering in the
620 backward half-space (blue dashed arrows), leading to a negative ARF.

621

622 **Fig. 2** (Color online) The coordinates relationship of the particle centroid [$O(0,0,0)$] and
623 beam origin [$O_B(x_0, y_0, z_0)$]. (x, y, z) is an arbitrary field point.

624

625 **Fig. 3** (Color online) Validations of the Axial ARFs calculated using the TMM compared
626 with those from the exact solutions for a rigid sphere ($a=b$) in a Bessel beam based on the
627 multipole expansion method. (a) On-axis incidence for with the orders $M=0$ (blue dashed
628 line) and $M=1$ (red solid line). (b) Off-axis incidences with the order $M=0$ and cone angle
629 $\beta=30^\circ$. (c) 2D schematic of a "peanut-shaped" generalized superspheroid placed on the
630 axis of a Bessel beam. (d) Convergence tests for a rigid generalized superspheroid with
631 aspect ratio $a/b = 4$ for on-axis and off-axis incidences with the order of Bessel beam
632 $M=1$.

633

634 **Fig. 4** (Color online) (a) The axial ARF of the rigid oblate spheroid with aspect ratio
635 $a/b = 1/2$ with $r_0 = b$ ($a < b$). The order of the Bessel beam is $M=1$ with cone angles

636 $\beta = 30^\circ$, 66.42° , and 80° . (b) Like panel (a) except that the particle is the prolate
637 spheroid with $a/b = 2$ and $r_0 = a$ ($a > b$). Panels (c) and (d) depict the enlarged view
638 of the negative ARF region for the rigid oblate and prolate spheroids, respectively. (e)
639 Angular dependence of the scattered form functions versus the scattered polar angle θ_s
640 for the oblate spheroid in the first-order HBB with $\beta = 80^\circ$ for $kr_0 = 1.8$ [red solid line,
641 corresponding to the red solid pentagram in (c)] and $kr_0 = 2.1$ [blue dash line,
642 corresponding to the blue solid pentagram in (c)]. The black dotted line denotes the
643 direction of the incident wave vector with $\theta_s = \beta$. Negative axial ARFs exist when the
644 scattering in the forward hemisphere is relatively stronger than that in the backward
645 hemisphere.

646

647 **Fig. 5** (Color online) Negative axial ARF “islands”. The 2D plots depict only the
648 negative ARFs in the (kr_0, β) domain with colors, while the white domain stands for the
649 non-negative ARFs. (a) the rigid generalized superspheroid with $a/b = 2$ under the
650 on-axis incidence of the OBB ($M=1$). (b) Like panel (a) except that order=1. (c) Like
651 panel (a) except that order=2. (d) Like panel (a) except that order=3. (e) Like panel (b)
652 except that $a/b = 3$. (f) Like panel (b) except that $a/b = 4$. (g) Like panel (c) except that
653 $a/b = 1/2$. $r_0 = b$ since $a < b$ in this case. This shape may model a red blood cell shape
654 with a dip in the center. Panels (h-l): The 2D negative ARF islands for a capsule shape
655 ($l=2b$) with $r_0 = l$. (h-j) are for the first-order ($M=1$) HBB with (h) on-axis and (i,j)

656 off-axis incidence. The offsets (x_0, y_0) in the unit of meters are $(0,0)$,
657 $(0.1\pi/kr_0, 0.1\pi/kr_0)$ and $(0.5\pi/kr_0, 0.5\pi/kr_0)$, respectively for (h-j). (k) Like panel (i)
658 except that order=2. (l) Like panel (j) except that order=2.

659

660 **Fig. 6** (Color online) Three-dimensional ARFs versus dimensional frequency kr_0 and
661 cone angle β . The first two columns describe the transverse ARFs while the third is the
662 axial ARFs. A rigid generalized superspheroid with aspect ratio $a/b = 2$ under the (a-c)
663 on-axis and (d-f) off-axis incidences of the first-order ($M=1$) HBB. The offset is set as
664 $(x_0, y_0) = (0.5\pi/kr_0, 0.5\pi/kr_0)$. The third row is as same as the second except that the
665 particle is a smoothed rigid spheroid with $a/b = 2$.

666

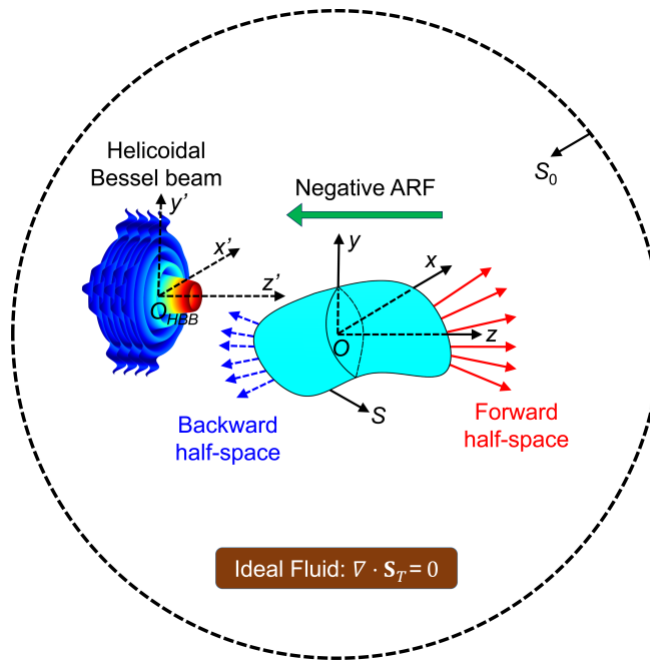
667 **Fig. 7** (Color online) Three-dimensional ARFs (first to third columns: Y_x , Y_y , and Y_z)
668 versus transverse offset x_0 and y_0 for Bessel beam with different orders: (a-c) OBB
669 ($M=0$); (d-f) first-order ($M=1$) HBB; (g-i) second-order ($M=2$) HBB.

670

671 **Fig. 8** (Color online) Axial ARFs of a rigid sphere in a standing or traveling Bessel beam
672 with a fixed cone angle $\beta = 60^\circ$.

673

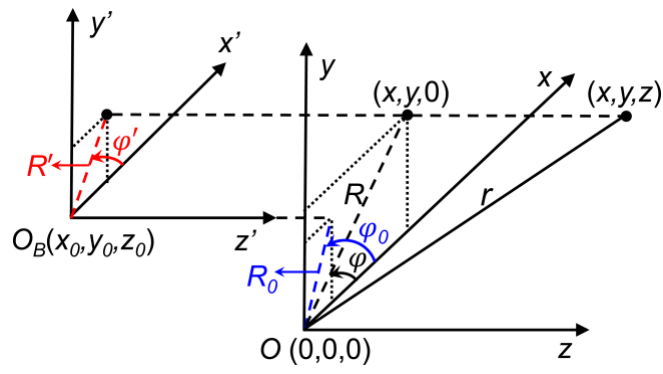
674 **Fig. 1**



675

676

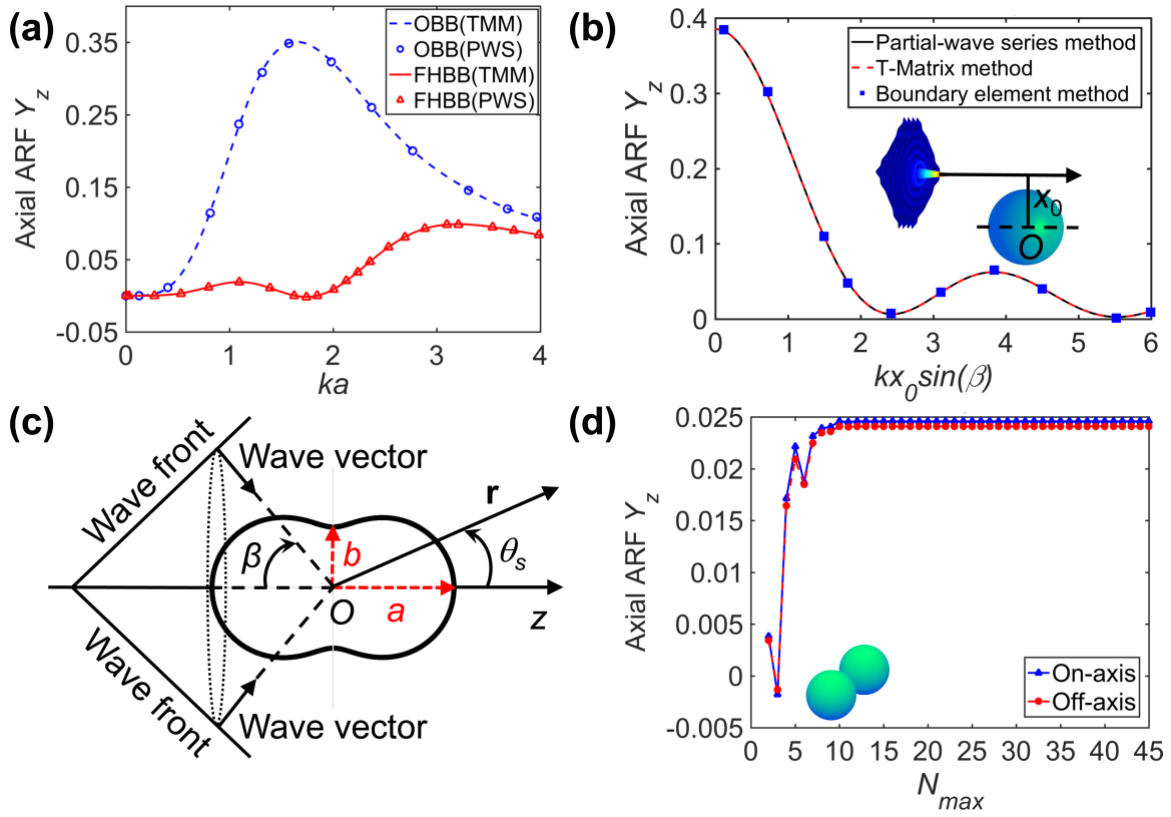
677 **Fig. 2**



678

679

680 **Fig. 3**

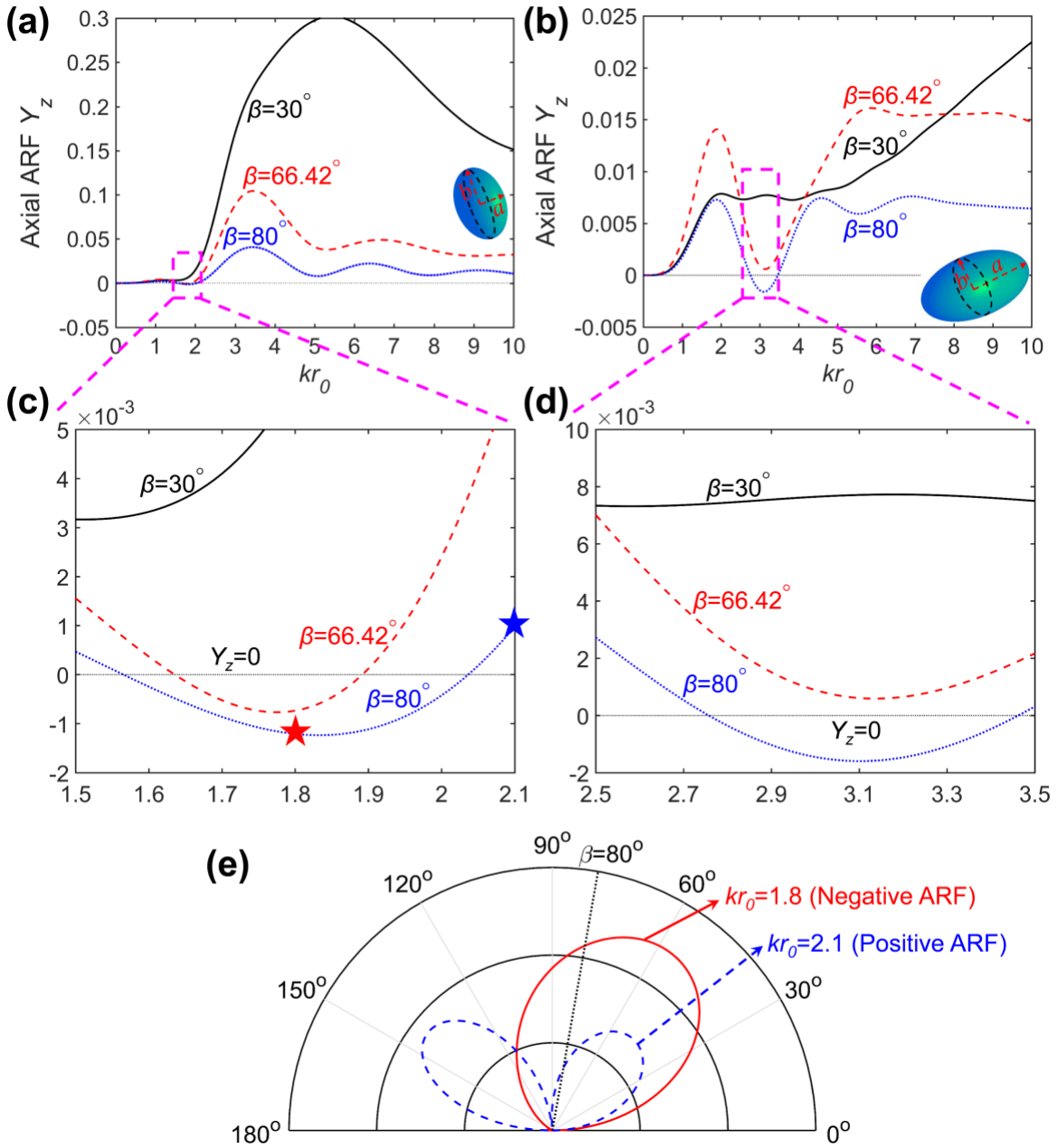


681

682

683

Fig. 4

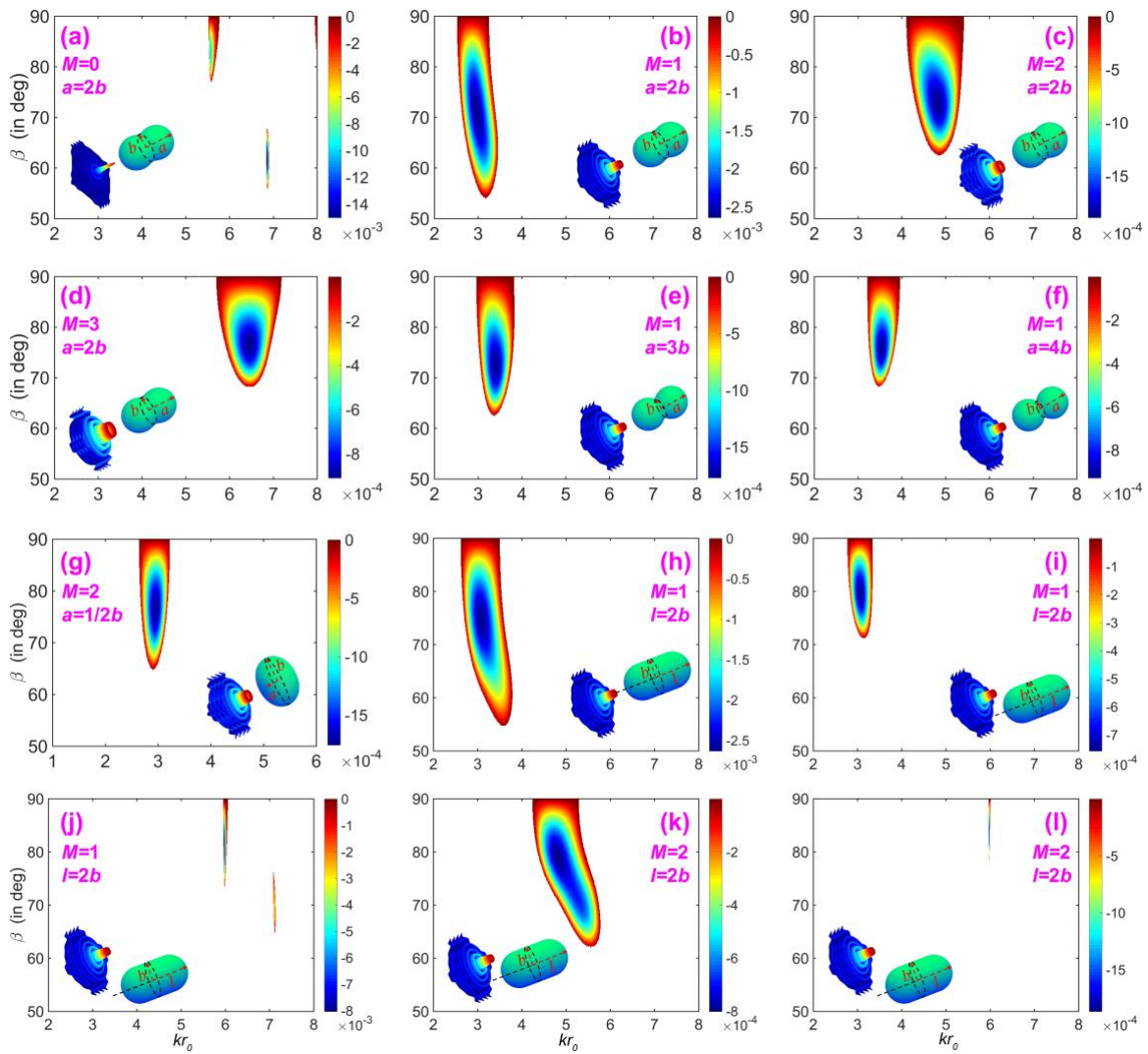


684

685

686

Fig. 5

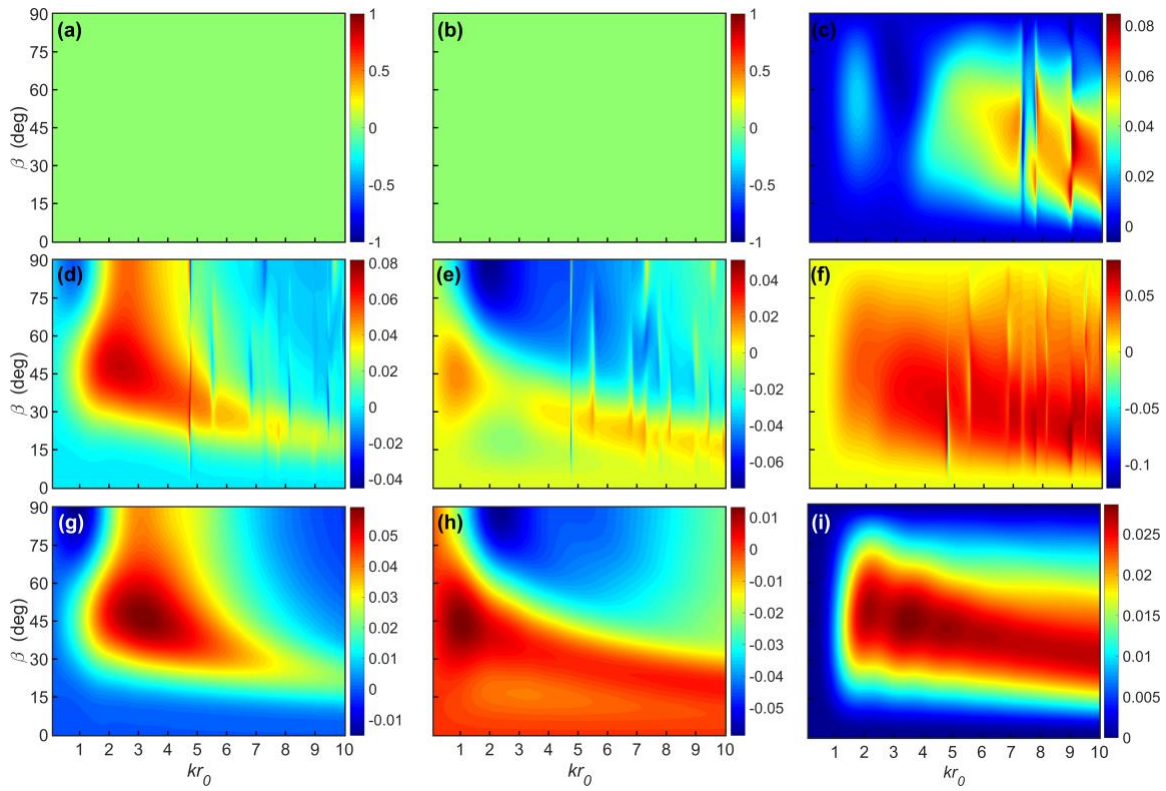


687

688

689

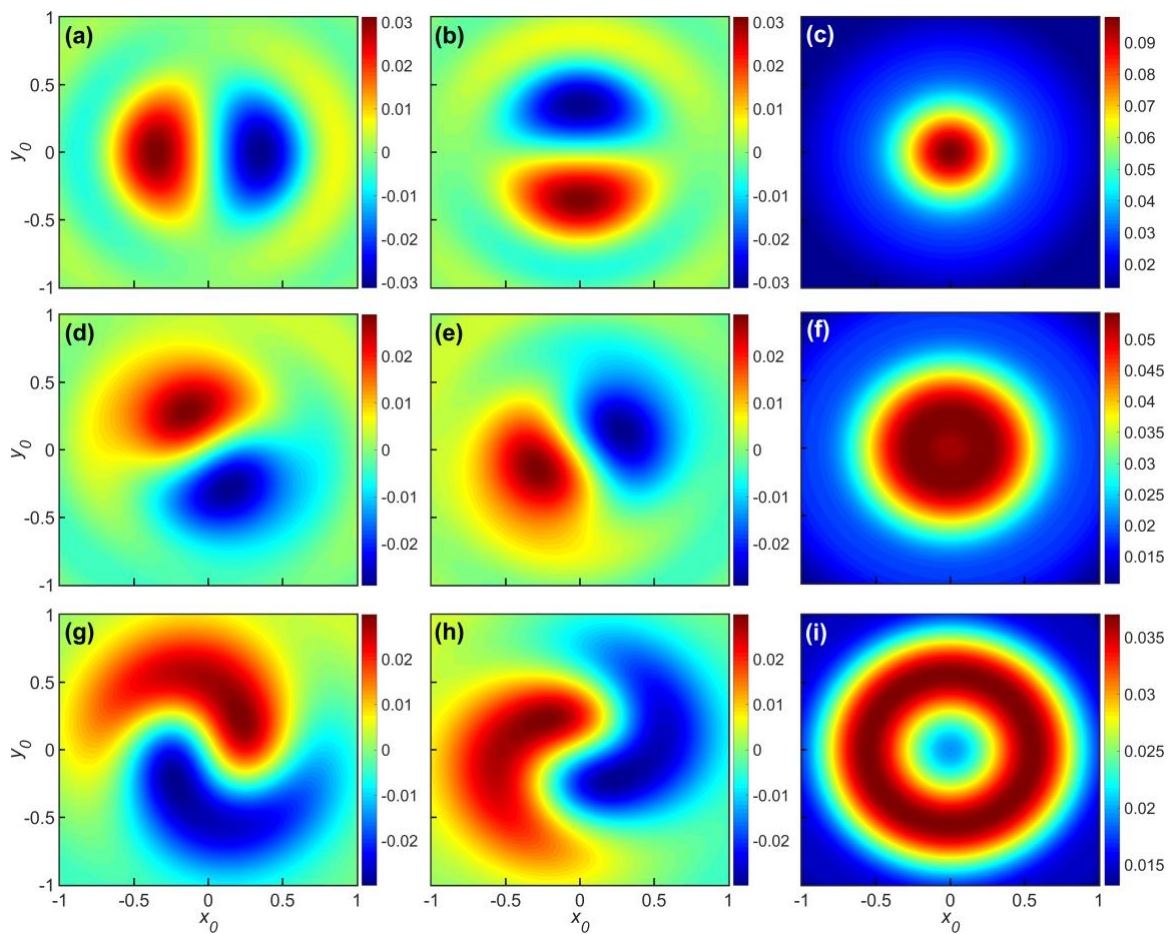
Fig. 6



690

691

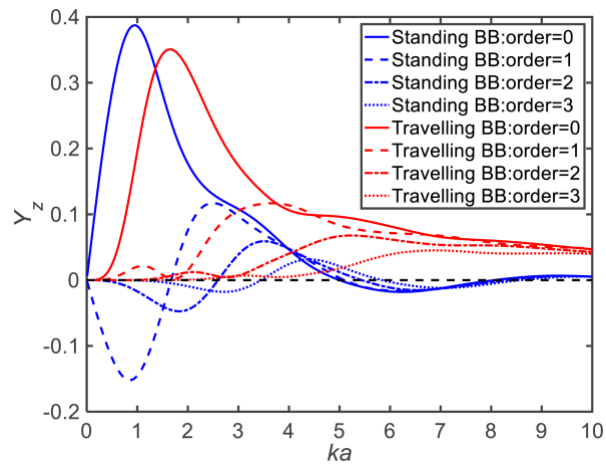
692 **Fig. 7**



693

694

695 **Fig. 8**



696